Spectral Imaging for Remote Sensing

Gary A. Shaw and Hsiao-hua K. Burke

Spectral imaging for remote sensing of terrestrial features and objects arose as an alternative to high-spatial-resolution, large-aperture satellite imaging systems. Early applications of spectral imaging were oriented toward ground-cover classification, mineral exploration, and agricultural assessment, employing a small number of carefully chosen spectral bands spread across the visible and infrared regions of the electromagnetic spectrum. Improved versions of these early multispectral imaging sensors continue in use today. A new class of sensor, the hyperspectral imager, has also emerged, employing hundreds of contiguous bands to detect and identify a variety of natural and man-made materials. This overview article introduces the fundamental elements of spectral imaging and discusses the historical evolution of both the sensors and the target detection and classification applications.

Of the five senses, vision plays a central role in human perception and interpretation of the world. When we hear a loud crash, smell something burning, or feel something slipping out of our grasp, our first response is visual—we *look* for the source of the trouble so we can assess and respond to the situation. Our eyes and brain can quickly provide detailed information about whatever event is occurring around us, which leads to a choice of appropriate action or response. The importance of human visual perception is also apparent when we consider that vision processing consumes a disproportionately large part of human brain function. It is therefore not surprising that, historically, much of our success in remote sensing, whether for civilian, military, terrestrial, or extraterrestrial purposes, has relied upon the production of accurate imagery along with effective human interpretation and analysis of that imagery.

Electro-optical remote sensing involves the acquisition of information about an object or scene without coming into physical contact with that object or scene. Panchromatic (i.e., grayscale) and color (i.e., red, green, blue) imaging systems have dominated electro-optical sensing in the visible region of the electromagnetic spectrum. Longwave infrared (LWIR) imaging, which is akin to panchromatic imaging, relies on thermal emission of the objects in a scene, rather than reflected light, to create an image.

More recently, passive imaging has evolved to include not just one panchromatic band or three color bands covering the visible spectrum, but many bands—several hundred or more—encompassing the visible spectrum and the near-infrared (NIR) and shortwave infrared (SWIR) bands. This evolution in passive imaging is enabled by advances in focal-plane technology, and is aimed at exploiting the fact that the materials comprising the various objects in a scene reflect, scatter, absorb, and emit electromagnetic radiation in ways characteristic of their molecular composition and their macroscopic scale and shape. If the radiation arriving at the sensor is measured at many wavelengths, over a sufficiently broad spectral band, the resulting spectral signature, or simply *spectrum,* can be used to identify the materials in a scene and discriminate among different classes of material.

While measurements of the radiation at many wavelengths can provide more information about the materials in a scene, the resulting imagery does not

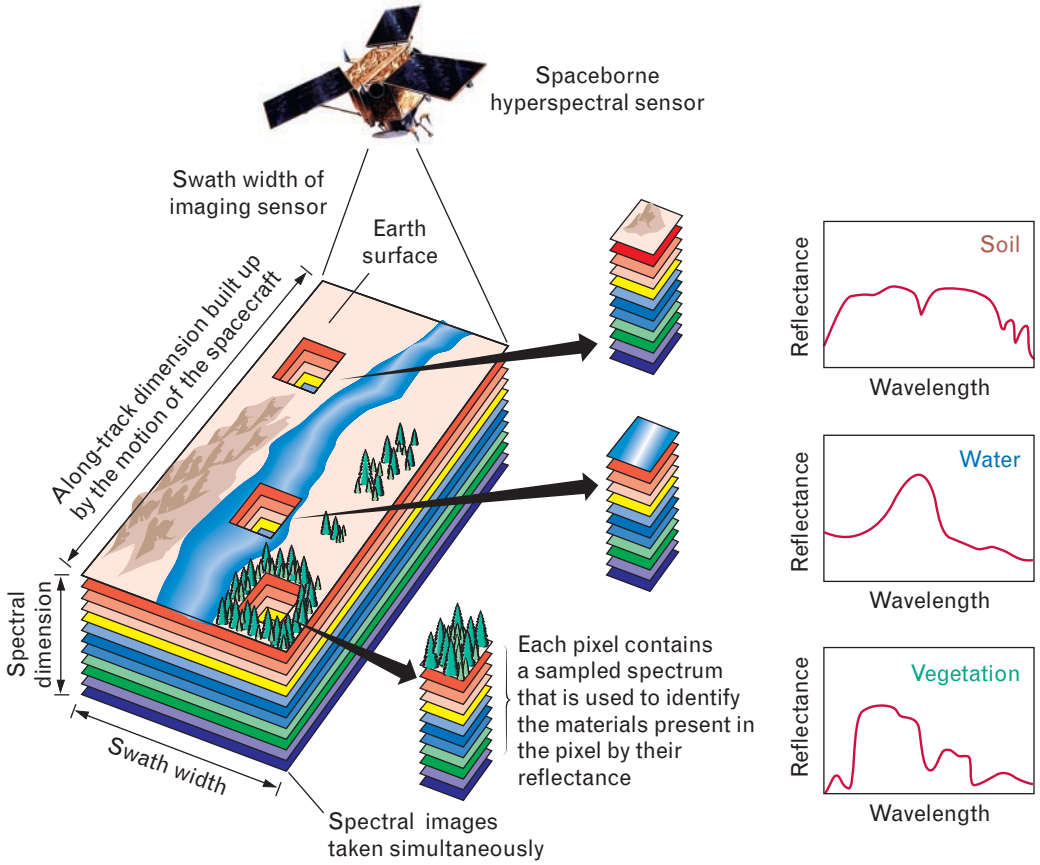

FIGURE 1. The concept of imaging spectroscopy. An airborne or spaceborne imaging sensor simultaneously samples multiple spectral wavebands over a large area in a ground-based scene. After appropriate processing, each pixel in the resulting image contains a sampled spectral measurement of reflectance, which can be interpreted to identify the material present in the scene. The graphs in the figure illustrate the spectral variation in reflectance for soil, water, and vegetation. A visual representation of the scene at varying wavelengths can be constructed from this spectral information.

lend itself to simple visual assessment. Sophisticated processing of the imagery is required to extract all of the relevant information contained in the multitude of spectral bands.

In this issue of the *Lincoln Laboratory Journal* we focus attention on spectral measurements in the solar-reflectance region extending from 0.4 to 2.5 μm, encompassing the visible, NIR, and SWIR bands. These three bands are collectively referred to as the VNIR/SWIR. The measurement, analysis, and interpretation of electro-optical spectra is known as *spectroscopy*. Combining spectroscopy with methods to acquire spectral information over large areas is known as *imaging spectroscopy.* Figure 1 illustrates the concept of imaging spectroscopy in the case of satellite remote sensing.

Fundamentals of Spectral Imaging

Throughout this special issue of the *Journal* we refer to the illumination conditions in a scene as well as the reflectance properties of materials and surfaces in that scene. *Irradiance* refers to the light energy per unit time (power) impinging on a surface, normalized by the surface area, and is typically specified in watts per square meter (W/m^2). *Reflectance* is a unitless number between 0 and 1 that characterizes the fraction of incident light reflected by a surface. Reflectance may be further qualified by parameters such as the wavelength of reflected light, the angle of incidence, and the angle of reflection. *Radiance* is an important related concept that does not distinguish between the light illuminating a surface or the light reflected from

a surface. Radiance is simply the irradiance normalized by the solid angle (in steradians) of the observation or the direction of propagation of the light, and is typically measured in W/m^2/steradian. Normalizing the radiance by the wavelength of the light, which is typically specified in microns (μm), yields *spectral radiance*, with units of W/m^2/μm/steradian.

Reflectance Spectrum

We are accustomed to using color as one of the ways we distinguish and identify materials and objects. The color and reflectivity of an object are typically important indications of the material composition of the object, since different materials absorb and reflect the impinging light in a wavelength-dependent fashion. To a first order, the reflected light, or spectral radiance $L_s(\lambda)$, that we see or that a sensor records is the product of the impinging scene radiance $L_i(\lambda)$ and the material reflectance spectrum $\rho(\lambda)$, both of which vary as a function of wavelength λ:

$$L_s(\lambda) = \rho(\lambda) L_i(\lambda). \qquad (1)$$

If the illumination spectrum is known, then the material reflectance spectrum, or *reflectivity*, can in principle be recovered from the observed spectral radiance over those regions of the spectrum in which the illumination is nonzero. Since the reflectance spectrum is independent of the illumination, the reflectance spectrum provides the best opportunity to identify the materials in a scene by matching the scene reflectance spectra to a library of known spectra.

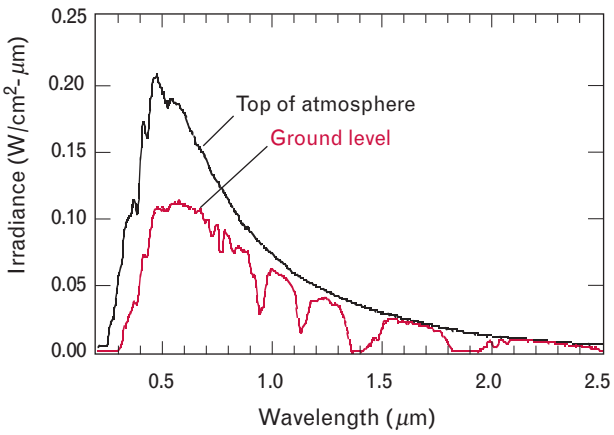

FIGURE 2. Solar spectral irradiance curves at the top of the atmosphere and at ground level. The solar irradiance outside the atmosphere (black curve) is well characterized. At ground level (red curve) it is altered by the absorption and scattering effects of the atmosphere. The recovery of reflectance spectra of different objects and materials must take into account the effects the atmosphere has on the spectrum of both the solar illumination and the reflected light.

In the case of solar illumination, the spectral irradiance of the light reaching the atmosphere is reasonably well characterized, as shown in Figure 2. Equation 1, however, oversimplifies the relation between reflectance and illumination. Many environmental and sensing phenomena can complicate the recovery of the reflectance spectra. For example, even though the spectrum of the solar radiation reaching the atmosphere is well characterized, the spectrum of the solar radiation reaching the ground is altered in a temporally and geographically dependent fashion because of propagation of solar radiation through the earth's constantly changing atmosphere. Such atmospheric modulation effects must be accounted for in order to reliably recover the reflectance spectra of materials on the ground in a sunlit scene.

Sensor errors can further impede the recovery of reflectance spectra by distorting and contaminating the raw imagery. For example, focal-plane vibration can result in cross-contamination of adjacent spectral bands, thus distorting the observed spectrum. A comprehensive discussion of sensor errors and artifacts is beyond the scope of this article. The next section, however, provides an overview of the image formation process.

Image Formation and Area Coverage Rate

Collecting two-dimensional spatial images over many narrow wavebands with a two-dimensional focal-plane imaging sensor typically involves some form of time-sequenced imaging. This collection can be accomplished by either a time sequence of two-dimensional spatial images at each waveband of interest, or a time sequence of spatial-spectral images (one-dimensional line images containing all the wavebands of interest), with multiple one-dimensional spatial images collected over time to obtain the second spatial dimension.

A variety of techniques have been developed to collect the required data. A common format for data collection is a push-broom imaging sensor, in which a

cross-track line of spatial pixels is decomposed into K spectral bands. Figure 3 illustrates the geometry for this type of data-collection system. The spectral decomposition can be accomplished by using any of several mechanisms, such as a diffraction grating or a wedge filter [1].

Historically, spectral imaging for remote sensing can be traced back to the Television Infrared Observation Satellite (TIROS) series first launched in 1960 [2]. The TIROS legacy has continued with the Advanced Very High Resolution Radiometer (AVHRR) and the Moderate Resolution Imaging Spectroradiometer (MODIS) instruments [3], launched aboard the Terra (Latin for *earth*) spacecraft in 1999. The spatial resolution of AVHRR is four kilometers, and the spatial resolution of the multispectral MODIS sensor varies from 250 meters in some spectral bands to one kilometer in others. In comparison, the focus of the articles in this issue of the *Journal* is on sensors with spatial resolutions better than thirty meters, and in some cases better than one meter.

Sampling

There are four sampling operations involved in the collection of spectral image data: spatial, spectral, radiometric, and temporal. In the systems discussed in this issue, we assume the spatial resolution is identical to the ground sample distance (GSD), although in general the GSD could be smaller than the spatial resolution. For the systems described in this issue, the GSD varies from a fraction of a meter to tens of meters, and is established primarily by the sensor aperture and platform altitude. Platform altitude is loosely constrained by the class of sensor platform (e.g., spaceborne versus airborne).

As noted earlier, spectral sampling is achieved by decomposing the radiance received in each spatial pixel into a number of wavebands. The wavebands may vary in resolution, and may be overlapping, contiguous, or disparate, depending upon the design of the sensor. A color image, consisting of red, green, and blue bands, is a familiar example of a spectral sampling in which the wavebands (spectral channels) are non-overlapping and relatively broad.

An analog-to-digital converter samples the radiance measured in each spectral channel, producing digital data at a prescribed radiometric resolution. The result is a three-dimensional spectral data cube, represented by the illustration in Figure 4. Figure 4(a) shows the spectra in cross-track scan lines being gathered by an airborne sensor. Figure 4(b) shows the scan lines being stacked to form a three-dimensional hyperspectral data cube with spatial information in the x and y dimensions and spectral information in the z dimension. In Figure 4(b) the reflectance spectra of the pixels comprising the top and right edge of the image are projected into the z dimension and color coded according to the amplitude of the spectra, with blue denoting the lowest-amplitude reflectance values and red denoting the highest values.

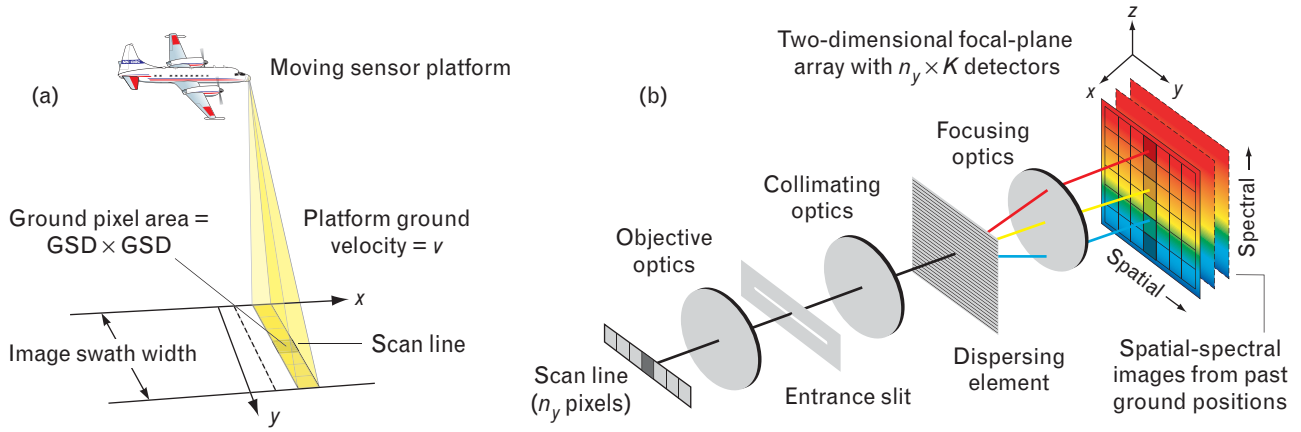

FIGURE 3. (a) Geometry of a push-broom hyperspectral imaging system. The area coverage rate is the swath width times the platform ground velocity v. The area of a pixel on the ground is the square of the ground sample distance (GSD). (b) An imaging spectrometer on the aircraft disperses light onto a two-dimensional array of detectors, with n_y elements in the cross-track (spatial) dimension and K elements in the spectral dimension, for a total of $N = K \times n_y$ detectors.

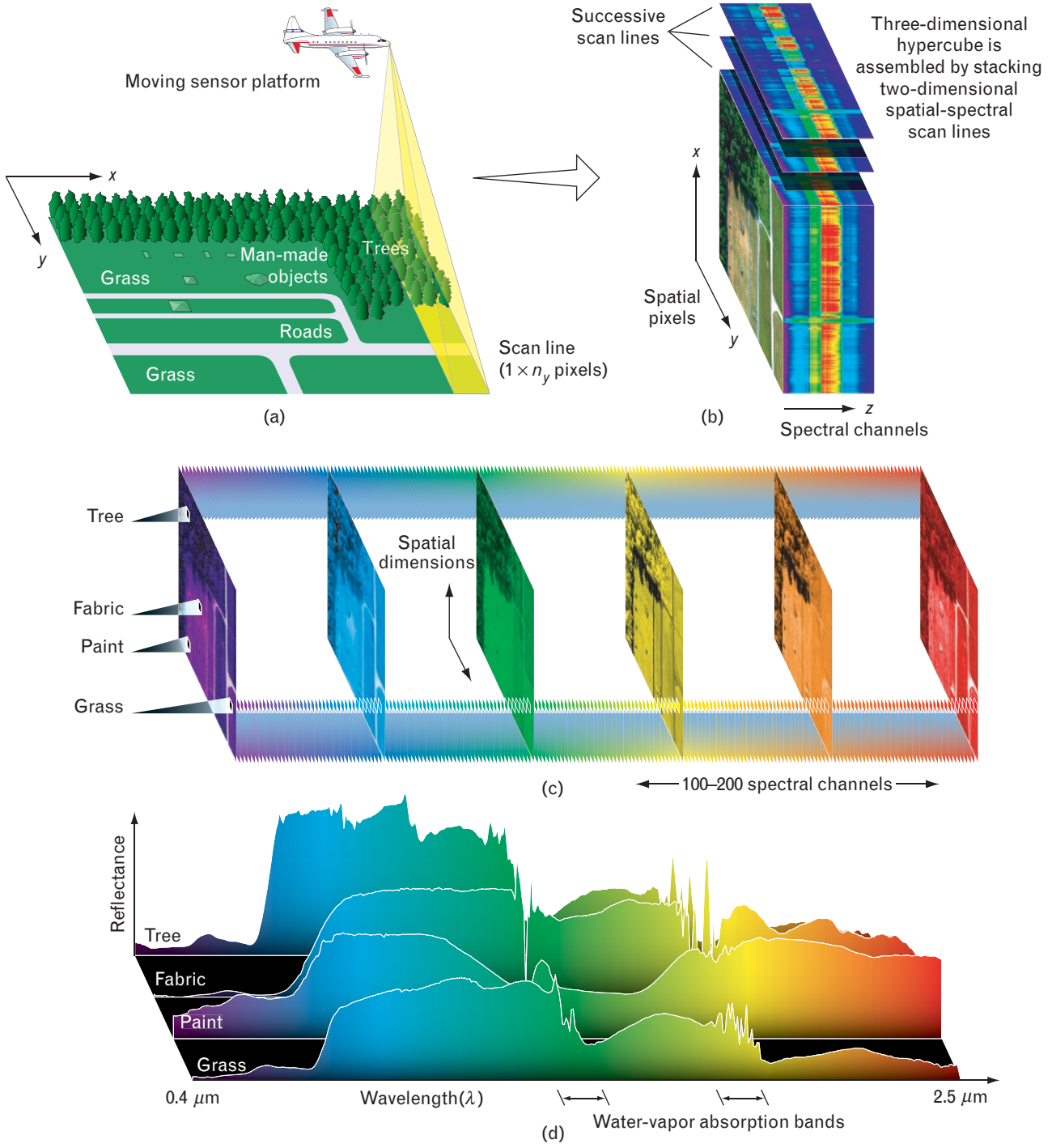

FIGURE 4. Structure of the hyperspectral data cube. (a) A push-broom sensor on an airborne or spaceborne platform collects spectral information for a one-dimensional row of cross-track pixels, called a *scan line*. (b) Successive scan lines comprised of the spectra for each row of cross-track pixels are stacked to obtain a three-dimensional hyperspectral data cube. In this illustration the spatial information of a scene is represented by the *x* and *y* dimensions of the cube, while the amplitude spectra of the pixels are projected into the *z* dimension. (c) The assembled three-dimensional hyperspectral data cube can be treated as a stack of two-dimensional spatial images, each corresponding to a particular narrow waveband. A hyperspectral data cube typically consists of hundreds of such stacked images. (d) Alternately, the spectral samples can be plotted for each pixel or for each class of material in the hyperspectral image. Distinguishing features in the spectra provide the primary mechanism for detection and classification of materials in a scene.

The spectral information in the z dimension might be sampled regularly or irregularly, depending on the design of the sensor. Spectral image data can be viewed as a stack of two-dimensional spatial images, one image for each of the sampled wavebands, as shown in Figure 4(c), or the image data can be viewed as individual spectra for given pixels of interest, as shown in Figure 4(d). (Note: In Figure 4, color in parts *c* and *d* represents spectral bands rather than reflectance amplitudes.)

While there is an integration time τ_d associated with the image formation process, we use the term *temporal sampling* to refer not to the time associated with image formation, but to the process of collecting multiple spectral images of the same scene separated in time. Temporal sampling is an important mechanism for studying natural and anthropogenic changes in a scene [4, 5].

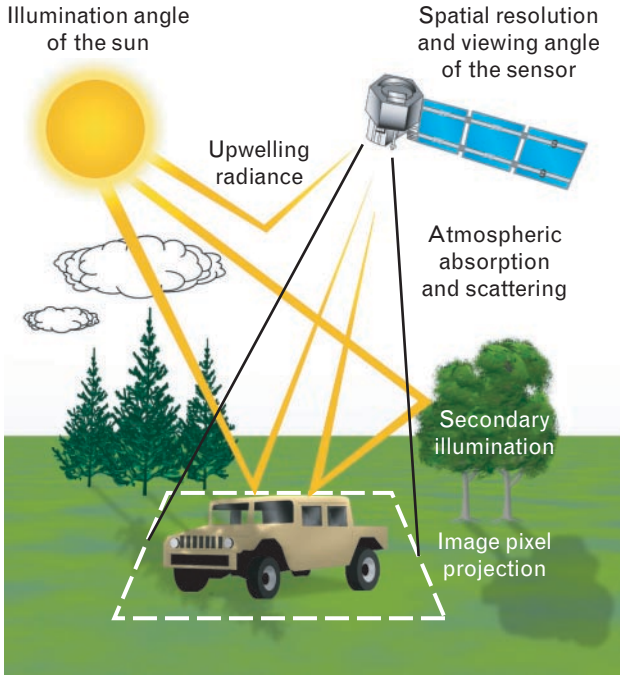

FIGURE 5. Atmospheric and scene-related factors that can contribute to degradations in the imaging process. The spatial resolution of the sensor and the degree of atmospheric scattering and absorption are the most significant contributors to diminished image quality.

Practical Considerations

The concept of spectral imaging, as illustrated in Figure 1, appears straightforward. There are many practical issues, however, that must be addressed in the design and implementation of a spectral imaging system. These issues include the spatial and spectral resolution of the sensor, atmospheric effects such as absorption and scattering, the spectral variability of surface materials in the scene, and other environmental effects such as viewing angle, secondary illumination, and shadowing. Figure 5 illustrates a number of these salient issues for a representative scene.

Spatial Resolution

Sensor cost is usually a strong function of aperture size, particularly for spaceborne systems. Reducing the aperture size reduces sensor cost but results in degraded spatial resolution (i.e., a larger GSD). For a spectral imager, the best detection performance is expected when the angular resolution of the sensor, specified in terms of the GSD, is commensurate with the footprint of the targets of interest. Targets, however, come in many sizes. Consequently, for a given sensor design, some targets may be fully resolved spatially, while others may fill only a fraction of the GSD footprint that defines a pixel. Therefore, detection and identification algorithms must be designed to function well regardless of whether targets are fully resolved (i.e., fully fill a pixel) or comprise only a fraction of the material in a given pixel (i.e., subpixel).

Atmospheric Effects

The atmosphere absorbs and scatters light in a wavelength-dependent fashion. This absorption and scattering has several important implications that cause difficulties for sensor imaging. Four of these difficulties are described below.

First, the atmosphere modulates the spectrum of the solar illumination before it reaches the ground, and this modulation must be known or measured in order to separate the spectrum of the illumination (the impinging solar radiance) from the reflectivity (the reflectance spectrum) that characterizes the materials of interest in the scene. Figure 6 shows the one-way total atmospheric transmission curve for two different water vapor and aerosol conditions, corresponding to extremes of wet and dirty versus clean and dry atmospheres. Figure 6 also shows the contri-

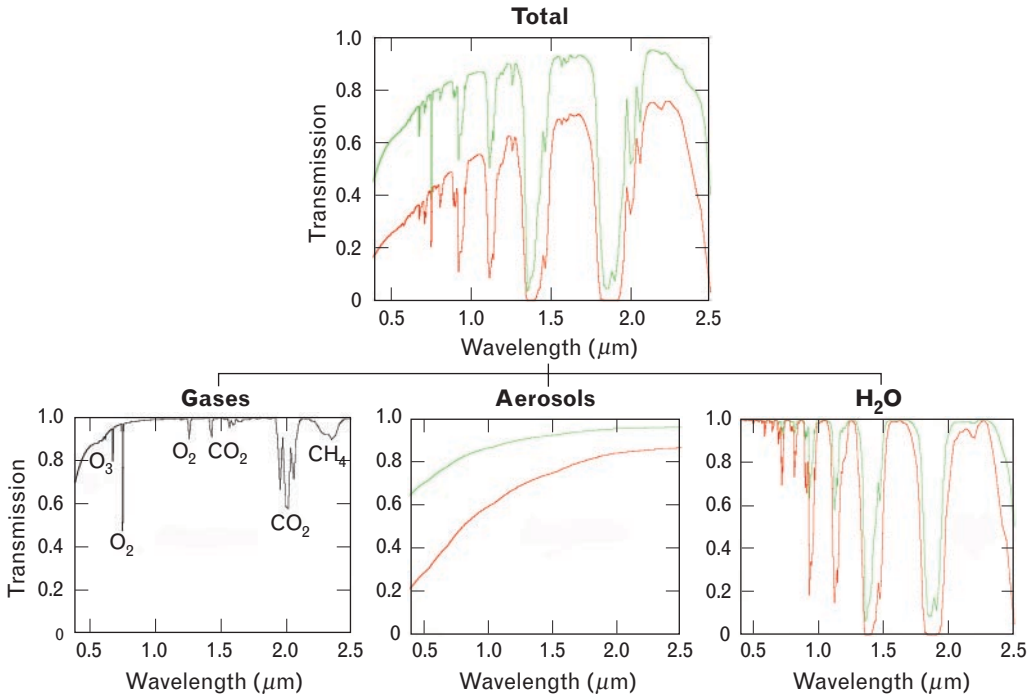

FIGURE 6. Effect of atmospheric gases, aerosols, and water vapor on total atmospheric transmission. The green curves represent the case of modest influence (0.4 cm col of water vapor), which corresponds to a rural environment with a visual range of 23 km. The red curves represent the case of strong influence (4.1 cm col of water vapor), which corresponds to an urban environment with a visual range of 5 km.

butions of well-mixed gases, aerosols, and water vapor to the overall transmission. As the solar-illumination angle and the viewing angle of the sensor change, the total path through the atmosphere changes, which in turn affects the total atmospheric transmission. Also, the water-vapor distribution (as well as the aerosol characteristics of the atmosphere) varies with location and time, so the methods of compensating for these effects must be scene based.

Second, some of the solar radiation is scattered by the atmosphere into the field of view of the sensor without ever reaching the ground. This scattered light is superimposed on the reflected light arriving from the scene, and is termed *path radiance* because it appears along the line-of-sight path to the scene. Third, the solar radiation scattered by the atmosphere, predominantly in the blue region of the visible spectrum, acts as a secondary source of diffuse colored illumination. This diffuse sky illumination is most important for shadowed objects, since regions shadowed from the direct rays of the sun may still be illuminated by the diffuse non-white sky radiation. Fourth, the solar illumination that reaches the scene and is reflected by the target is further absorbed and scattered by the atmosphere as it propagates toward the sensor.

A number of methods are currently used to estimate and compensate for these atmosphere propagation effects. The appendix entitled "Fundamentals of Atmospheric Compensation" provides additional detail on these compensation methods.

Other Environmental Effects

In addition to atmospheric absorption and scattering, several other prominent environmental parameters and associated phenomena have an influence on spectral imaging. The sun angle relative to zenith, the sensor viewing angle, and the surface orientation of the target all affect the amount of light reflected into the sensor field of view. Clouds and ground cover may cast shadows on the target, substantially changing the illumination of the surface. Nearby objects may also reflect or scatter sunlight onto the target, superimposing various colored illuminations upon the dominant direct solar illumination, as illustrated in Figure 5.

Spectral Variability

Early in the development of spectral imaging, researchers hypothesized that the reflectance spectrum of every material is unique and, therefore, represents a means for uniquely identifying materials. The term "spectral signature," which is still in use today, suggests a unique correspondence between a material and its reflectance spectrum. In field data, however, as well as laboratory data, we observe variability in the reflectance spectrum of most materials. Many mechanisms may be responsible for the observed variability, including uncompensated errors in the sensor, uncompensated atmospheric and environmental effects, surface contaminants, variation in the material such as age-induced color fading due to oxidation or bleaching, and adjacency effects in which reflections from nearby objects in the scene change the apparent illumination of the material. Seasonal variations also introduce enormous changes in the spectral character of a scene. We need only observe the changes in a deciduous forest over spring, summer, fall, and winter to appreciate the degree of spectral variability that can arise in the natural materials comprising a scene.

There is some reason to expect that man-made materials exhibit less spectral variability than the naturally occurring materials in a scene. Figure 7 shows a number of instances of reflectance spectra derived for multiple occurrences of fully resolved vehicle-paint pixels in a scene. Note that while the shapes of the spectra are fairly consistent, the amplitude varies considerably over the scene. In an effort to exploit the spectral shape invariance, some of the more successful detection algorithms give more weight to the spectral shape than to the amplitude when determining whether a particular material is present in a pixel.

Motion and Sensor Artifacts

As indicated in Figure 3, spectral imaging sensors typically exploit sensor platform motion as a means of scanning a scene. However, nonlinear motion of the sensor can corrupt the spectral image by mixing together the spectral returns from different parts of the spatial image. Motion of objects in the scene can also create artifacts if the motion is on the order of the GSD during the integration time τ_d. This type of spatial migration can degrade image quality, but fortunately it is not as significant as the spectral migration in terms of impact on subsequent processing for detection and identification of materials. The imaging of a scene, including detection and conversion of the radiance to a digital sequence, introduces a number of artifacts such as thermal noise, quantization, and geometric distortion. The nature of these sensor artifacts, and methods for modeling them, are discussed in more detail in the article entitled "Hyperspectral Imaging System Modeling," by John P. Kerekes and Jerrold E. Baum.

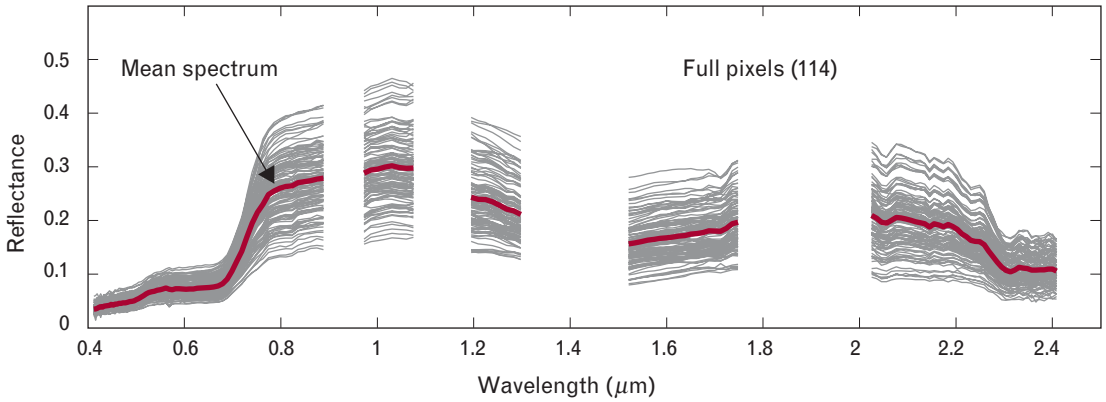

FIGURE 7. Example of variability in reflectance spectra measured over multiple instances of a given material (in this case, vehicle paint) in a scene. The shapes of the spectra are fairly consistent, but the amplitudes vary considerably over the scene. To exploit this spectral shape invariance, some detection algorithms give more weight to the spectral shape than to the spectral amplitude in determining whether a given material is present in a pixel. The gaps correspond to water-vapor absorption bands where the data are unreliable and are discarded.

Spatial versus Spectral Information

The emergence of radar sensors in the late 1930s opened the door to detection and discrimination of radar-reflecting targets without relying on traditional spatial imagery. Less than sixteen years after the introduction of the first operational radar, however, researchers were flying experimental side-looking airborne radars (SLAR) in order to transform radar returns into images [6]. Synthetic aperture radar (SAR) was devised to create images from two-dimensional range-Doppler radar reflectance maps [7]. Interferometric SAR was developed later as a means of generating three-dimensional radar images [8]. The introduction of light detection and ranging (lidar) technology provided another way to create three-dimensional images in the form of high-resolution angle-angle-range reflectance maps. Throughout the evolution of passive and active imaging methods, improved spatial resolution has been a mantra of development that has pushed optical sensors to larger apertures and radar sensors to higher frequencies. Automated detection and recognition algorithms have evolved along with these sensors, but human visual analysis continues to be the predominant means of interpreting the imagery from operational imaging sensors.

Multispectral Imaging

Increasing the spatial resolution of imaging sensors is an expensive proposition, both in terms of the sensor and in terms of the amount of sensor data that must subsequently be processed and interpreted. The trained human analyst has traditionally carried the main burden of effective image interpretation, but as technology continues to advance, the volume of high-resolution optical and radar imagery has grown at a faster rate than the number of trained analysts.

In the 1960s, the remote sensing community, recognizing the staggering cost of putting large passive imaging apertures in space, embraced the concept of exploiting spectral rather than spatial features to identify and classify land cover. This concept relies primarily on spectral signature rather than spatial shape to detect and discriminate among different materials in a scene. Experiments with line-scanning sensors providing up to twenty spectral bands in the visible and infrared were undertaken to prove the concepts [9]. This experimental work helped create interest and support for the deployment of the first space-based multispectral imager, Landsat-1 [10], which was launched in 1972 (Landsat-1 was originally designated the Earth Resource Technology Satellite, or ERTS 1). Landsat-7, the latest in this series of highly successful satellites, was launched in 1999. A Lincoln Laboratory prototype for a multispectral Advanced Land Imager (ALI) was launched in November 2000 aboard the National Aeronautics and Space Administration (NASA) Earth Observing (EO-1) satellite [11]. EO-1 also carries a VNIR/SWIR hyperspectral sensor, called Hyperion, with 220 spectral bands and a GSD of thirty meters.

Hyperspectral Imaging

On the basis of the success of multispectral sensing, and enabled by advances in focal-plane technology, researchers developed hyperspectral sensors to sample the expanded reflective portion of the electromagnetic spectrum, which extends from the visible region (0.4 to 0.7 μm) through the SWIR (about 2.5 μm) in hundreds of narrow contiguous bands about ten nanometers wide. The majority of hyperspectral sensors operate over the VNIR/SWIR bands, exploiting solar illumination to detect and identify materials on the basis of their reflectance spectra.

If we consider the product of spatial pixels times spectral bands (essentially the number of three-dimensional resolution cells in a hypercube) to be a measure of sensor complexity, then we can preserve the overall complexity in going from a panchromatic sensor (with one broad spectral band) to a hyperspectral sensor (with several hundred narrow spectral bands) by reducing the number of spatial pixels by a factor of several hundred while keeping the field of view constant. In effect, a one-dimensional reduction in spatial resolution by a factor of approximately fifteen (i.e., the square root of K, the number of spectral bands, which is typically about 220) compensates for the increased number of spectral samples and reduces the required aperture diameter by the same factor, thus reducing the potential cost of a sensor. However, while the total number of three-dimensional resolu-

tion cells is preserved, the information content of the image is generally not preserved when making such trades in spatial versus spectral resolution.

Area Coverage Rate

In many cases, a primary motivation for applying spectral imaging to remote sensing is to reduce the required spatial resolution—and thus the size and weight—of the sensor. Therefore, it is worthwhile, even in this brief overview, to consider the design trade-offs involved in selecting the spatial and spectral resolution of a spectral imaging sensor. Table 1 summarizes the important spectral image formation parameters in this discussion.

When the achievable signal-to-noise ratio (SNR) is limited by the imaging process in the sensor and not by noise (interference) in the scene, the SNR^2 of the sensor grows in proportion to the product of the receive aperture area d^2, the area of a pixel on the ground (which for the purpose of this simple analysis we equate to the square of the GSD), the time interval τ_d over which the signal is integrated at the detector, and the scene radiance L_s at the sensor:

$$\mathrm{SNR}^2 \propto d^2 \times \mathrm{GSD}^2 \times \tau_d \times L_s . \qquad (2)$$

The integration time is proportional to the GSD divided by the platform velocity v:

$$\tau_d \propto \frac{\mathrm{GSD}}{v}.$$

In a spectral imaging sensor, the radiance signal from each pixel is decomposed into K spectral bands, so that the average spectral radiance L_λ in each spectral band (detector) on the focal plane is

$$L_\lambda \propto \frac{L_s}{K}.$$

Substituting for τ_d in Equation 2, and absorbing the scene-radiance scale factor into the proportionality sign, the SNR proportionality at the detector can be expressed as

$$\mathrm{SNR}^2 \propto \frac{d^2 \times \mathrm{GSD}^3}{v \times K}. \qquad (3)$$

To relate this expression to area coverage rate (ACR), we note from Figure 3 that the swath width (SW) is equal to the GSD times the number of cross-track samples:

$$\mathrm{SW} = \mathrm{GSD} \times (N/K),$$

where N is the total number of detectors in the focal plane. Therefore, Equation 3 can be rewritten as

$$\mathrm{SNR}^2 \propto \frac{d^2 \times N \times \mathrm{GSD}^4}{\mathrm{SW} \times v \times K^2}.$$

The achievable ACR is then given by

$$\mathrm{ACR} \equiv \mathrm{SW} \times v \propto \frac{d^2 \times N \times \mathrm{GSD}^4}{\mathrm{SNR}^2 \times K^2}.$$

By fixing the aperture size d and the number of detectors N on the focal plane, we find that the ACR is proportional to the square of the ground sample area, and inversely proportional to both the square of the SNR and the square of the number of spectral bands:

$$\mathrm{ACR} \propto \frac{\mathrm{GSD}^4}{\mathrm{SNR}^2 \times K^2}. \qquad (4)$$

Spatial versus Spectral Trade-Space Example

The expression for ACR given in Equation 4 can be evaluated to further quantify the trade-off between spectral and spatial resolution. Consider, as a baseline for comparison, a panchromatic imaging system (K = 1), with GSD = 0.3 m, SNR = 100, and ACR = 30 km^2/hr. In the following comparison we consider

Table 1. Spectral Image Formation Parameters

Aperture diameter	d
Image swath width	SW
Integration time	τ_d
Number of cross-track elements	n_y
Number of spectral channels	K
Number of detectors in focal plane	$N (= n_y \times K)$
Scene radiance	L_s
Sensor platform velocity	v
Ground sample distance	GSD

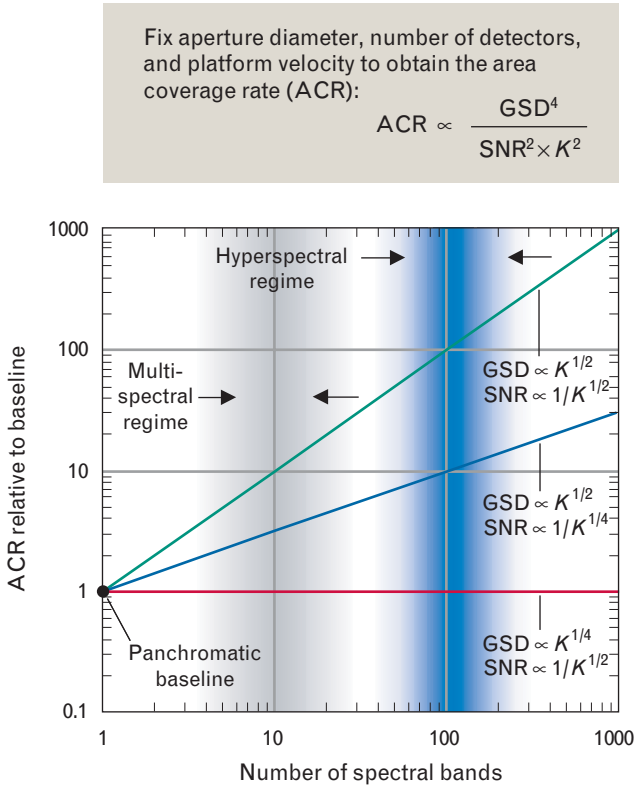

	1 band	10 bands	100 bands
GSD	0.3 m	1 m	3 m
SNR*	100	32	10
ACR	30 km²/hr	300 km²/hr	3000 km²/hr
GSD	0.3 m	1 m	3 m
SNR*	100	56	32
ACR	30 km²/hr	100 km²/hr	300 km²/hr
GSD	0.3 m	0.5 m	1 m
SNR*	100	32	10
ACR	30 km²/hr	30 km²/hr	30 km²/hr

*SNR in this table represents the average SNR per spectral band

FIGURE 8. Example of trade space for spatial, spectral, and area coverage rate (ACR). The plot on the left shows the improvement in ACR that can be achieved with a multiband spectral sensor by trading spatial resolution for spectral resolution. The baseline reference system is a single-band panchromatic imager with a resolution of 0.3 m and an ACR of 30 km²/hr. The red curve represents the family of multiband imagers that achieve the same ACR as the baseline by simultaneously reducing the spatial resolution (i.e., increasing GSD) and the SNR in an individual detector. The GSD and SNR for a single-band panchromatic system, a 10-band multispectral system, and a 100-band hyperspectral system are shown in the red box in the table to the right. The blue and green curves correspond to other trades in which the ACR of the multiband sensor is increased relative to the panchromatic baseline. The table again provides specific values of GSD, SNR, and ACR for the case of a 10-band multispectral system and a 100-band hyperspectral system.

a 10-band system to be representative of a multispectral sensor, and a 100-band system to be representative of a hyperspectral system.

According to Equation 4, increasing the number of spectral bands while maintaining the GSD and detector SNR constant results in a decrease in ACR. Since a primary rationale for multispectral and hyperspectral imaging is to reduce reliance on high spatial resolution for detection and identification, the ACR can be preserved while increasing the number of spectral bands by increasing the GSD (i.e., reducing the spatial resolution). According to Equation 4, one way to preserve the ACR when increasing the spectral bands by K is to reduce the GSD by a factor of $K^{1/2}$. However, since each pixel is decomposed into K bands, detection processing such as matched filtering, which combines the K bands for detection, can yield an improvement in SNR of $K^{1/2}$, which is the gain from noncoherent integration of K samples. Therefore, it makes sense to reduce the SNR in each detector by $K^{1/2}$ and increase the GSD by a smaller amount. An increase in GSD by $K^{1/4}$ and a decrease in SNR by $K^{1/2}$ preserves the overall ACR. A decrease in the pixel SNR by $K^{1/2}$ along with an increase in GSD by $K^{1/2}$ increases the ACR by a factor of K, relative to the baseline panchromatic sensor. Figure 8 shows these spectral-versus-spatial trades and the impact on ACR.

In Figure 8 the performance of the baseline panchromatic sensor (one spectral band) is represented by the convergence of the three curves at the normalized ACR of 1.0. As more spectral bands are added, the ACR can be preserved by letting the GSD grow in

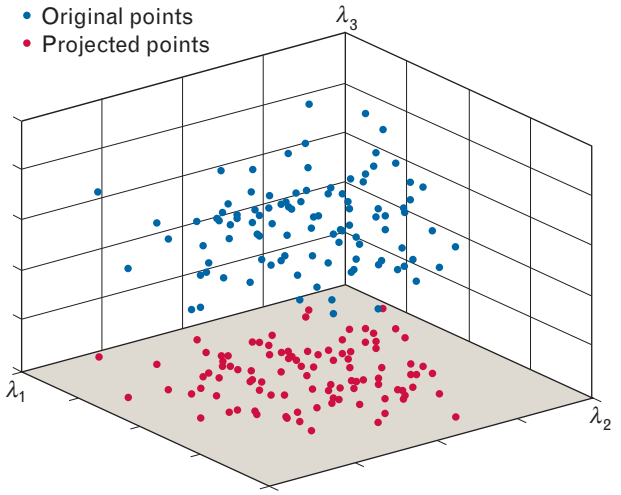

FIGURE 9. Example of data from a multispectral image sensor with only three wavebands, λ_1, λ_2, and λ_3. In this three-dimensional example, the wavelength-dependent reflectivity of a material is measured in each of the three wavebands and used to characterize the material. If a number of different materials are measured, each material can be represented as a data point in a three-dimensional space, as indicated by the blue dots. Dimensionality reduction of the data is illustrated by projecting the data cloud into a lower dimensional space defined by the (λ_1, λ_2) plane. The projected data, represented by red dots, still preserve the uniqueness of the original data points, although the separation in Euclidean distance between the data points is reduced.

proportion to $K^{1/4}$ while the detector SNR is allowed to decrease in proportion to $1/K^{1/2}$, as represented by the red curve. The companion table shows examples of the resulting GSD and SNR for the cases when K = 10 and K = 100, corresponding to representative multispectral and hyperspectral sensors. The blue curve represents a design trade in which the ACR is increased by a factor of $K^{1/2}$ over the panchromatic baseline. Note from the table that the factor of $K^{1/2}$ = 10 improvement in ACR for K = 100 is achieved at the cost of an SNR reduction per detector of $K^{1/4}$ = 3.2. Matched filtering of the spectral information in a pixel may compensate for much of the reduction in SNR within the individual detectors.

High-Dimensional Data Representation

The manner in which spectral image data are processed is strongly influenced by the high dimensionality of the data. To illustrate the concept of data dimensionality, we consider a multispectral image sensor with only three wavebands, λ_1, λ_2, and λ_3. As in the high-dimensional case, the wavelength-dependent reflectivity of a material is used to characterize the material. For this low-dimensional example, if a number of different materials are measured, each material can be represented as a data point in a three-dimensional space, as indicated by the blue dots in Figure 9. Each unique point in this space represents a spectral signature defined by the 3-tuple (λ_1, λ_2, λ_3). The spectral signature is thus seen as a vector of length—or dimension—three. This representation is highly compatible with many numerical processing algorithms.

Dimensionality Reduction

Depending upon the nature of the data, it may be possible to project the data cloud into a lower dimensional space while still preserving the separation and uniqueness of the data points. Figure 9 illustrates this process, in which the three-dimensional representation (indicated by blue dots) is projected onto a two-dimensional plane (indicated by red dots), thus reducing the dimensionality by one. If two or more of the blue dots project onto the same point in the two-dimensional plane, it is no longer possible to distinguish the projected blue points as unique. In general, finding a projection that preserves the relevant information content of the data (separation) while reducing dimensionality is a complicated undertaking. The article in this issue by Nirmal Keshava entitled "A Survey of Spectral Unmixing Algorithms" describes this topic in greater detail.

The same concept of dimensionality illustrated in Figure 9 can be applied to hyperspectral sensors with hundreds of contiguous spectral wavebands. Unlike the three-dimensional example, all the information contained in a high-dimensional data cloud cannot be visualized by a two-dimensional or three-dimensional perspective plot. At best, we can construct two-dimensional and three-dimensional visualizations by projecting the K-dimensional spectral vector into an appropriately chosen two-dimensional or three-dimensional subspace.

An important implication of the dimension-reduction example is that, unlike conventional panchromatic and color imagery, higher-dimension hyper-

spectral imagery requires computer processing for maximum information extraction and visualization. This processing can be totally automated or it can be accomplished with guidance from an image analyst. After processing is completed, the information can be highlighted, perhaps with pseudocolor, and displayed in a two-dimensional image, but the computer-processing step is an essential precursor to visualization.

How Many Dimensions Are Needed?

If the task is to discriminate between a particular target material and a particular class of background, a few well-chosen wavebands are usually sufficient to separate the target and background materials. If this is true, we might well question the motivation for hyperspectral sensing, in which hundreds of contiguous narrow wavebands are measured by the sensor. Different materials, however, exhibit different spectral features. Certain paints and vegetation can be characterized by broad, slowly varying spectral features. Other materials, such as minerals and gases, possess very narrow spectral features, and the location of these narrow features in the spectral band differs for each class of material. Therefore, narrow wavebands may be needed to resolve features that help differentiate similar spectra, and contiguous bands are needed to handle the expected variety of materials, since important features may be in different spectral locations for each material. In addition, the narrow wavebands that straddle the water-vapor absorption bands are important in estimating and correcting for the variable water vapor contained in the atmosphere.

Thus, if we were interested in only a few target materials and backgrounds, a limited number of carefully chosen narrow wavebands would suffice to recover the salient spectral features. As more types of targets and backgrounds are added to the list, however, the number and location of wavebands needed to discriminate between any given spectral pair grows rapidly. One possible solution would be to build many special-purpose sensors, each of which collects only a minimal set of wavebands needed for a limited set of targets and backgrounds. A more cost-effective and robust solution is to build one type of sensor that oversamples the spectral information, and to develop application-specific algorithms, or a family of algorithms, that remove the redundant or undesired spectral information while preserving the information relevant to a given application. The essence of hyperspectral processing for detection and identification of materials is the extraction of salient features and the suppression of redundant or common features.

Spectral Imaging Applications

By oversampling the spectral information, we can apply hyperspectral imaging sensors to a variety of distinctly different problems, adapting the processing used to extract relevant information. There is much value, however, in tailoring the spatial resolution and sensor field of view for the intended class of application. Higher spatial resolution provides an improved signal-to-background-interference ratio for spatially small targets, usually at the cost of decreased sensor field of view. In general, the spatial resolution of the sensor is chosen on the basis of the spatial extent of the primary targets of interest. Figure 10 presents a simplified taxonomy of the many different types of hyperspectral imaging applications, identifying three major categories: anomaly detection, target recognition, and background characterization.

Anomaly Detection

Anomaly detection is characterized by the desire to locate and identify uncommon features in an image. These features could be man-made materials dispersed in a natural background, or they could be departures of the natural features from the norm. One of the early applications of multispectral imaging was to detect the spread of corn blight in the Midwest [10]. This application depends primarily on being able to distinguish brown withered leaves interspersed in fields of healthy green corn stalks.

Target Recognition

Target recognition is distinguished from anomaly detection by the availability of some *a priori* information about the target. This information could be a library of spectral reflectance signatures associated with targets, or less explicit information such as a reflectance signature extracted from within the scene. For example, anomaly detection could be used to isolate specific materials in a scene, and subsequent passes of

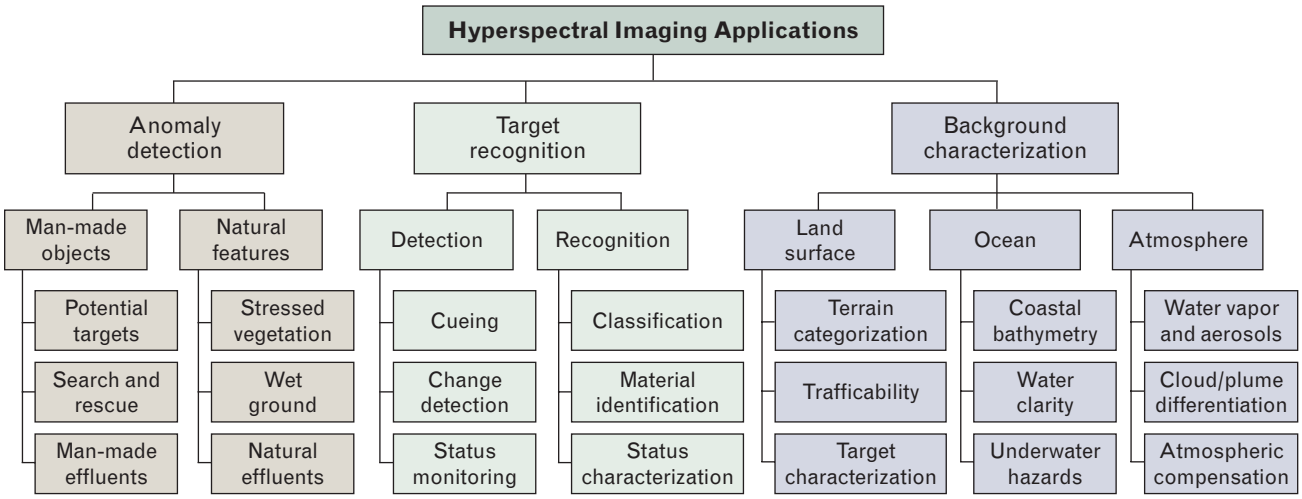

FIGURE 10. Simplified taxonomy of applications for hyperspectral imaging. The three major application categories are anomaly detection, target recognition, and background characterization. Anomaly detection divides pixels into man-made objects or natural features, target recognition provides detection parameters along with classification parameters of potential targets, and background characterization identifies the condition of natural features associated with land, ocean, or atmosphere.

an imaging sensor might be used to search for similar materials as well as to verify that the previously detected objects or materials have not moved. With a spectral library, materials might be identified and associated with specific types of targets, thus providing a form of target recognition.

Background Characterization

The first two application categories listed in Figure 10 emphasize detection and identification of spatially isolated features in an image, in the form of anomalies or targets. The third category emphasizes overall background scene analysis and identification, and spans the domains of land, ocean, and atmosphere. Because the Landsat imaging program has operated for over thirty years, much of the spectral image data collected to date has been oriented toward land characterization, employing multispectral sensors with GSD values of thirty meters or more.

An example of background scene characterization is coastal characterization, including shallow-water bathymetry. The sidebar entitled "Hyperspectral versus Multispectral Remote Sensing for Coastal Characterization" illustrates the evolution of multispectral sensors for this application and shows examples of the information products that can be derived from multispectral and hyperspectral data.

Spectral Processing

As implied in the previous section, the number and variety of applications for hyperspectral remote sensing are potentially quite large. However, the majority of algorithms used in these applications can be organized according to the following primitive application-specific tasks: (a) searching the pixels of a hyperspectral data cube for rare spectral signatures (*anomaly detection* or *target detection*); (b) finding the significant (i.e., important to the user) changes between two hyperspectral scenes of the same geographic region (*change detection*); (c) assigning a label or class to each pixel of a hyperspectral data cube (*classification*); and (d) estimating the fraction of the pixel area occupied by each material present in the pixel (*unmixing*). Note that from a signal processing perspective, task *c* (labeling pixels) is a classification problem, whereas task *d* (determining the constituent elements of a pixel) is an estimation problem.

Preliminary Processing to Reduce Dimensionality

Raw data from the sensor must usually undergo a series of calibration and correction operations to compensate for artifacts and gain variations in the sensor. The result is a calibrated radiance cube, which may be processed directly, or it may have atmospheric com-

pensation applied to it to produce a reflectance cube. Once a calibrated data cube is produced, dimensionality reduction of the data prior to application of detection or classification algorithms can lead to significant reductions in overall computational complexity. Reducing data dimensionality also reduces the number of pixels required to obtain accurate estimates of statistical parameters, since the number of samples (pixels) required to obtain a statistical estimate with a given accuracy is generally proportional to some power of the data dimensionality. The most widely used algorithm for dimensionality reduction is principal-component analysis (PCA), which is the discrete analog to the Karhunen-Loève transformation for continuous signals. The PCA algorithm is described in more detail in the article in this issue entitled "Enhancing Hyperspectral Imaging System Performance with Sensor Fusion," by Su May Hsu and Hsiao-hua K. Burke.

Figure 11 is a simplified block diagram of the spectral processing chain, starting with a calibrated radiance cube, and illustrating the common elements of atmospheric compensation and dimensionality reduction. Subsequent specialized processing depends on the intended application. Figure 11 illustrates two of many possible applications, *unmixing* and *detection*, each of which is discussed briefly in the following sections and developed more fully in companion articles in this issue.

Classification versus Detection

Formally, classification is the process of assigning a label to an observation (usually a vector of numerical values), whereas detection is the process of identifying the existence or occurrence of a condition. In this sense, detection can be considered as a two-class classification problem: target exists or target does not exist. Traditional classifiers assign one and only one label to each pixel, producing what is known as a thematic map. This process is called *hard classification*. The need to deal more effectively with pixels containing a mixture of different materials, however, leads to the concept of *soft classification* of pixels. A soft classifier can assign to each pixel multiple labels, with each label accompanied by a number that can be interpreted as the likelihood of that label being correct or, more generally, as the proportion of the material within the pixel.

In terms of data products, the goal of target-detection algorithms is to generate target maps at a con-

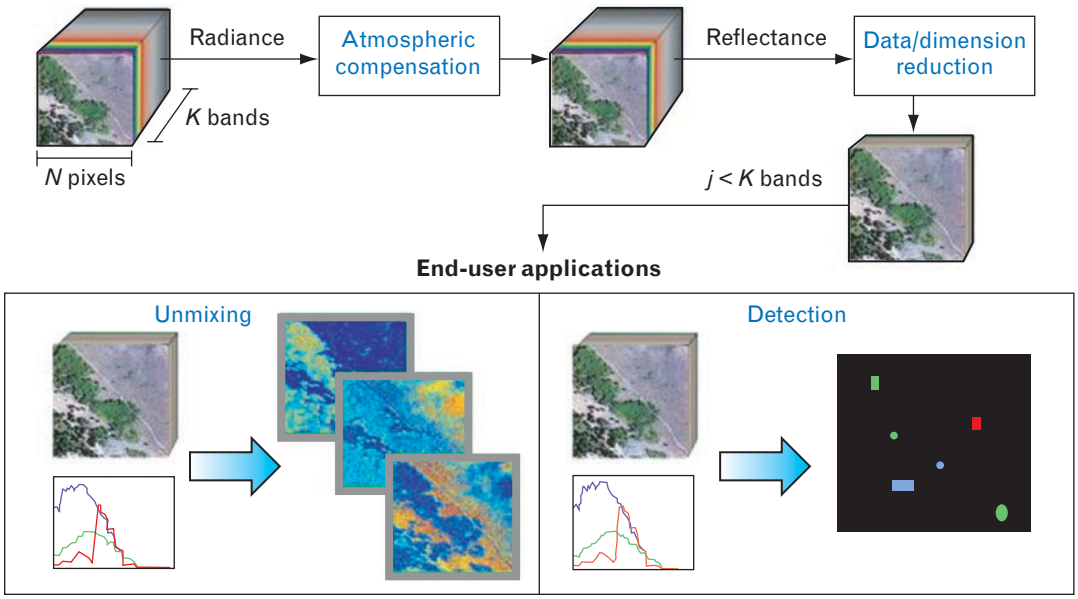

FIGURE 11. Simplified spectral processing diagram. The spectral processing typically starts with calibration of the data cube, followed by atmospheric compensation and dimensionality reduction. Subsequent specialized processing is determined by the intended end-user application, such as unmixing or detection.

HYPERSPECTRAL VERSUS MULTISPECTRAL REMOTE SENSING FOR COASTAL CHARACTERIZATION

OCEANS COMPRISE two-thirds of the earth's surface. The optical properties of ocean water are influenced by many factors, such as phytoplankton, suspended material, and organic substances. Spectral remote sensing provides a means of routinely monitoring this part of our planet, and obtaining information on the status of the ocean.

Ocean waters are generally partitioned into open ocean and coastal waters. Phytoplankton is the principal agent responsible for variations in the optical properties of open ocean. Coastal waters, on the other hand, are influenced not just by phytoplankton and related particles, but also by other substances, most notably inorganic particles in suspension and organic dissolved materials. Coastal characterization is thus a far more complex problem for optical remote sensing.

Figure A illustrates a variety of multispectral ocean color sensors used in the past twenty-five years. The spectral bands of these sensors, which lie in the spectral range between 0.4 and 1.0 μm, were chosen to exploit the reflection, backscatter, absorption, and fluorescence effects of various ocean constituents. These multispectral sensors vary in the number of bands and exact band loca-

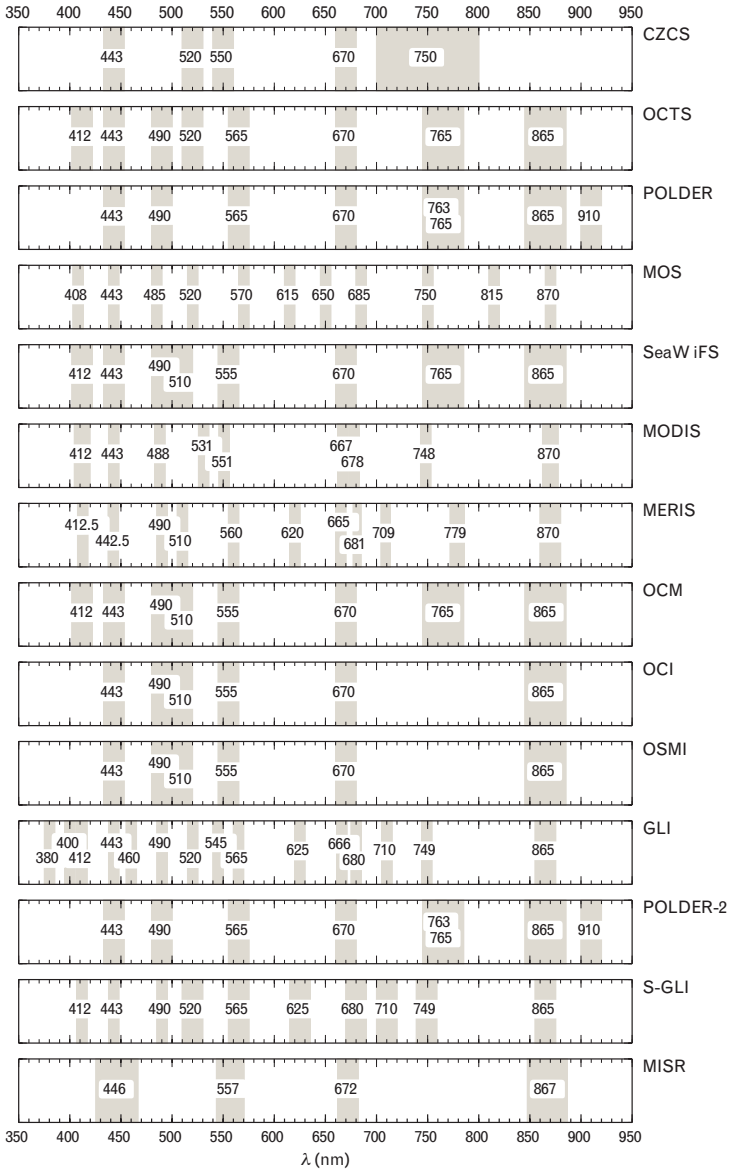

FIGURE A. Spaceborne multispectral ocean sensors from 1976 to the present, showing the numbers and locations of spectral bands. The variety of bands indicates the ocean characteristics the sensors are designed to investigate. (Figure courtesy of the International Ocean Colour Coordinating Group, taken from IOCCG Report no. 1, 1998.)

tions. The variety of bands and bandwidths in the sensors of Figure A indicates the lack of consensus on what the "best" bands are. Even though these multispectral sensors have routinely provided products for analysis of materials in the open ocean, their success with coastal water characterization has been limited because of the limited numbers of spectral bands. Complex coupled effects in coastal waters between the atmosphere, the water column, and the coastal bottom are better resolved with hyperspectral imaging. Physics-based techniques and automated feature-extraction approaches associated with hyperspectral sensor data give more information to characterize these complex phenomena.

Figure B illustrates some of the sample products over coastal regions. Hyperspectral sensors covering the spectral range between 0.4 and 1 μm include the necessary bands to compare with legacy multispectral sensors. Hyperspectral sensors can also gather new information not available from the limited numbers of bands in legacy systems.

Furthermore, even though most ocean-characterization algorithms utilize water-leaving radiance, the atmospheric aerosol effect is most pronounced in shortwave visible regions where ocean color measurements are made. With contiguous spectral coverage, atmospheric compensation can be done with more accuracy and precision.

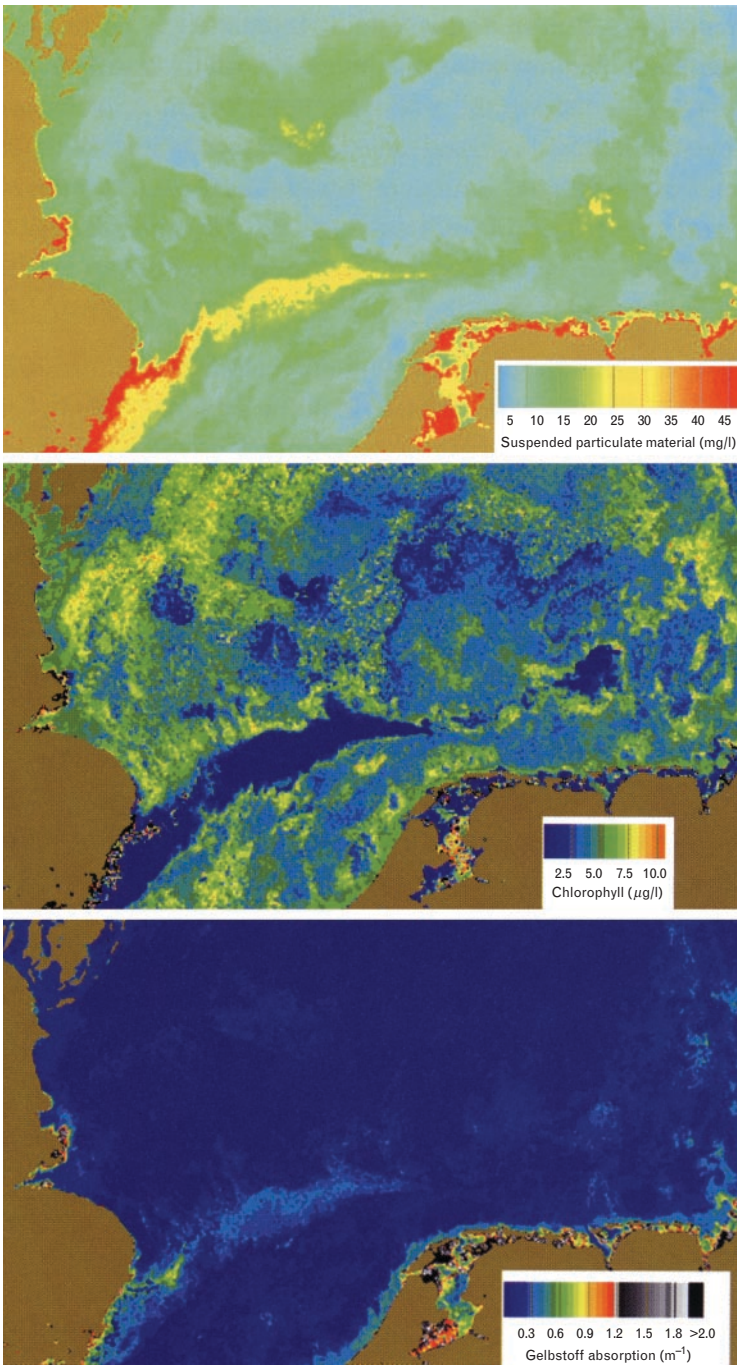

FIGURE B. Distribution of suspended matter (top), chlorophyll concentration (middle), and absorption by colored dissolved organic matter in the North Sea (bottom). These coastal ocean products are representative examples of multispectral remote sensing. With hyperspectral sensor data, these products can be retrieved more accurately because of better atmospheric correction and decoupling of complex phenomena. (Figure courtesy of the International Ocean Colour Coordinating Group, taken from IOCCG Report no. 3, 2000.)

stant false-alarm rate (CFAR), which is a highly desirable feature of these algorithms. Change-detection algorithms produce a map of significant scene changes that, for reliable operation, depend upon the existence of a reliable CFAR change-detection threshold. The hard or soft thematic maps produced by these CFAR algorithms convey information about the materials in a scene, and this information can then be used more effectively for target or change detection.

The thematic-map approach is not feasible for target detection applications because of the lack of training data for the target. At first glance, detection and classification look deceptively similar, if not identical. However, some fundamental theoretical and practical differences arise because of the rarity of the target class, the desired final product (target detection maps versus thematic maps), and the different cost functions (misclassifying pixels in a thematic map is not as critical as missing a target or overloading a target tracking algorithm with false alarms). CFAR detection algorithms are discussed more fully in the article entitled "Hyperspectral Image Processing for Automatic Target Detection Applications," by Dimitris Manolakis, David Marden, and Gary A. Shaw.

Unmixing

As noted in the discussion of spatial resolution, since materials of interest (i.e., targets) may not be fully resolved in a pixel, there is value in being able to decompose the spectral signature from each pixel in a scene into the individual collection of material spectra comprising each pixel. The development of algorithms to extract the constituent spectra comprising a pixel, a process called *unmixing*, has been aggressively pursued only during the last decade. In contrast to detection and classification, unmixing is an estimation problem. Hence it is a more involved process and extracts more information from the data. The article in this issue entitled "A Survey of Spectral Unmixing Algorithms," by Nirmal Keshava, discusses in greater depth the issues associated with unmixing.

Scene Illumination

The overall quality of passive imagery, and the success in extracting and identifying spectral signatures from multispectral or hyperspectral imagery, both depend heavily on the scene illumination conditions. As noted previously, illumination within a scene can vary significantly because of shadows, atmospheric effects, and sun angle. In fact, at many latitudes, the lack of adequate solar illumination prohibits reliable spectral reflectance imaging for a large portion of a twenty-four-hour day. An obvious solution to this problem is to provide active controlled illumination of the scene of interest. Achieving this simple goal, however, requires much more sophistication than we might first imagine.

During peak months, solar illumination reaching the earth's surface can be 800 W/m^2 or more, concentrated in the visible region of the spectrum. With the NASA Jet Propulsion Laboratory (JPL) Airborne Visible Infrared Imaging Spectrometer (AVIRIS) hyperspectral sensor [12] as an example, to artificially create this level of continuous illumination over the 17-m × 11-km swath comprising an AVIRIS scan line would require on the order of 150 MW of optical power, which is clearly impractical. Several steps can be taken to reduce the required power for illumination. The projection of the instantaneous field of view of the sensor on the ground can be reduced in area. This reduction can be achieved by narrowing the angular field of view of the sensor, or by moving the sensor closer to the scene, or a combination of the two. Since the area decreases in proportion to the square of the range and the square of the angular field of view, decreasing each by a factor of ten would reduce the required illumination power by a factor of 10,000.

The intensity of the artificial illumination can also be reduced, relative to natural solar illumination, but this requires the sensor and associated processing to operate at lower SNRs. A reduction of an order of magnitude over peak solar illumination may be possible, depending upon the scene being illuminated. The decrease in illumination intensity could be achieved either by a uniform reduction in optical power or by selectively reducing illumination in discrete wavebands. For example, with a multispectral sensor, there is no value in illuminating wavebands that are outside the sensor's detection bands. Another way to reduce the total illumination energy is to pulse the illumination in much the same fashion as a flash unit on a camera.

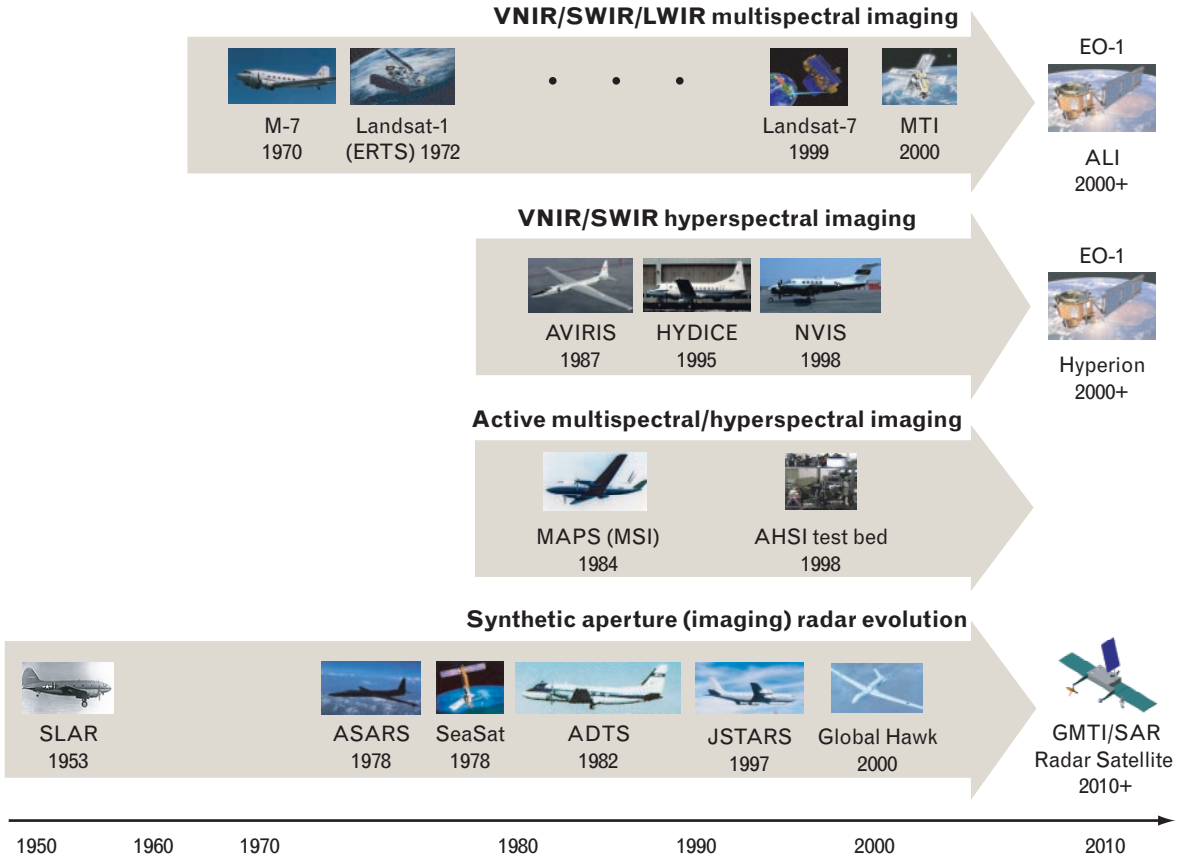

FIGURE 12. Timeline highlighting development of three different categories of spectral imaging, along with parallel developments in synthetic aperture radar (SAR) imaging. The uppermost timeline represents the evolution of multispectral sensing from airborne experiments through the series of Landsat satellite imagers, culminating in the Advanced Land Imager (ALI) experiment flown on NASA's Earth Observing (EO-1) satellite. The second timeline illustrates that high-spatial-resolution (≤ 30 m) hyperspectral sensing has been implemented on a number of experimental airborne platforms, including the Hyperspectral Digital Imagery Collection Experiment (HYDICE) and the Airborne Visible Infrared Imaging Spectrometer (AVIRIS). EO-1 also carries a hyperspectral sensor called Hyperion in addition to the multispectral ALI sensor. The third timeline shows that active multispectral and hyperspectral sensing to date is limited to a few research efforts.

Through a combination of reduced standoff range, reduced field of view, lower operating SNR, and pulsed band-selective illumination, it is possible to actively illuminate scenes for multispectral and hyperspectral sensors. An early example of such a sensor was the Lincoln Laboratory Multispectral Active/Passive Sensor (MAPS), which included active pulsed laser illumination at 0.85 μm and 10.59 μm, as well as an 8-to-12-μm thermal imager [13]. More recent work, discussed in the article entitled "Active Spectral Imaging," by Melissa L. Nischan, Rose M. Joseph, Justin C. Libby, and John P. Kerekes, extends the active image concept to the hyperspectral regime by using a novel white-light pulsed laser for illumination.

Spectral Imaging Chronology and Outlook

Interesting parallels exist in the development of radar imaging and spectral imaging, and in hyperspectral imaging in particular. Figure 12 displays milestones in the development of multispectral and hyperspectral airborne and spaceborne sensors. Highlights in the development of SAR imaging are also included at the bottom of the figure for comparison. The first operational radar system—the Chain Home Radar—commenced operation in Britain in 1937. Less than sixteen years later, in 1953, side-looking SAR radar experiments were under way in the United States. Work on airborne SAR eventually led to the develop-

Table 2. Comparison of Hyperspectral Imaging Systems

Parameter	*HYDICE*	*AVIRIS*	*Hyperion*
Nominal altitude (km)	1.6	20	705
Swath (km)	0.25	11	7.6
Spatial resolution (m)	0.75	20	30
Spectral coverage (μm)	0.4–2.5	0.4–2.5	0.4–2.5
Spectral resolution (nm)	7–14	10	10
Number of wavebands	210	224	220
Focal-plane pixels (spatial × spectral)	320 × 210	614 × 224	256 × 220
Data-cube size	300 × 320 × 210	512 × 614 × 224	660 × 256 × 220
Cube collection time (sec)	~3	43	3

ment and launch by NASA in 1978 of the experimental spaceborne Seasat SAR. Exactly a quarter of a century elapsed between the initial demonstration of airborne side-looking SAR and the launch of the spaceborne Seasat SAR.

In comparison, one of the first successful airborne multispectral scanning imagers, the Environmental Research Institute of Michigan (ERIM) M-7, was demonstrated in 1963. Twenty-four years later, in 1987, the first airborne hyperspectral imager, called AVIRIS, was commissioned. AVIRIS was the first earth-looking imaging spectrometer to cover the entire solar-reflectance portion of the spectrum in narrow contiguous spectral channels. Thirteen years after the commissioning of AVIRIS, the first spaceborne hyperspectral sensor, called Hyperion, was launched into orbit on the EO-1. The thirty-four-year time lag between the first airborne SAR in 1953 and the first airborne hyperspectral imager in 1987, and the twenty-two-year lag between the launch of Seasat and Hyperion, suggest that hyperspectral imaging is following a development timeline similar to that of SAR, but is a few decades less mature.

By borrowing from the work on algorithms and the lessons learned in radar and multispectral sensor development, there is reason to believe that the more than twenty-year maturity gap between SAR imaging and hyperspectral imaging can be closed quickly. In comparison to the twenty-five-year gap between the first airborne SAR and the launch of a spaceborne SAR, the gap of only thirteen years between AVIRIS, the first airborne hyperspectral sensor, and the spaceborne Hyperion is an encouraging sign that hyperspectral technology is maturing rapidly.

Table 2 summarizes this overview of spectral imaging systems, comparing the salient features of three hyperspectral sensors—the Hyperspectral Digital Imagery Collection Experiment (HYDICE) [14], AVIRIS, and Hyperion [15]—referenced in Figure 12. Note that the sensors span a range of altitudes and GSD values. Figure 13 (not drawn to scale) compares the ground swath widths of the sensors, illustrating the trade-off among spatial resolution, ACR, and altitude. Figure 13 also shows the swath width of Landsat-7, which precedes EO-1 in orbit by one minute. The data from these and other sensors afford the remote sensing community an opportunity to refine and enhance algorithms and application concepts.

In This Issue

This issue of the *Journal* contains six articles that discuss areas of spectral image research at Lincoln Laboratory. The first article, "Compensation of Hyperspectral Data for Atmospheric Effects," by Michael K. Griffin and Hsiao-hua K. Burke, deals with the important issue of atmospheric, or more generally, envi-

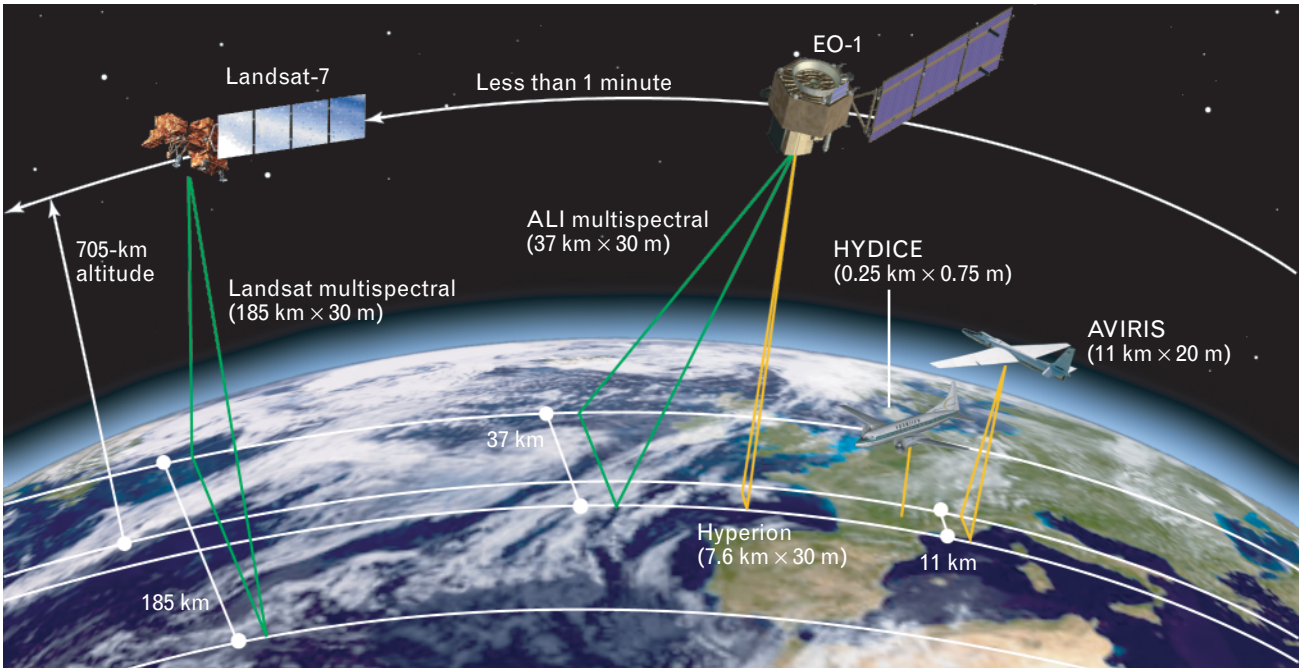

FIGURE 13. Altitude and area coverage regimes for HYDICE, AVIRIS, and Hyperion (on EO-1) hyperspectral sensor platforms. The nominal swath width and spatial resolution of each sensor are shown in parentheses. Note the difference in swath width between the mature operational Landsat-7 multispectral sensor (185 km) and the experimental hyperspectral sensors—HYDICE (0.25 km), AVIRIS (11 km), and Hyperion (7.6 km).

ronmental compensation and characterization. Algorithms that seek to detect or identify materials by spectral signature must account for the effects of the environment, including solar illumination, atmospheric attenuation and scattering, and shadowing. To the user who seeks spectral signatures within an image, the atmospheric artifacts are a nuisance that must be removed. To the atmospheric scientist, however, these artifacts provide a wealth of information about changes in atmospheric gases and aerosols.

The second article, "A Survey of Spectral Unmixing Algorithms," by Nirmal Keshava, deals with a broad class of algorithms that are central to unraveling the information contained in a hyperspectral signal. Since a given pixel in a hyperspectral image can be comprised of many materials, methods have been devised to estimate the number as well as the types of materials in a pixel, along with the relative fraction of the pixel area that each material occupies. This estimation problem is generally referred to as unmixing.

The third article, "Hyperspectral Image Processing for Automatic Target Detection Applications," by Dimitris Manolakis, David Marden, and Gary A. Shaw, deals with the automatic detection of spatially resolved and spatially unresolved targets in hyperspectral data. Relative to the traditional problem of land classification, the use of hyperspectral imagery for target detection places new demands on processing and detection algorithms. Targets are generally sparse in the imagery, with too few target pixels to support statistical methods of classification. In addition, a mistake in declaring a target when none is present (a false alarm) can be costly in terms of subsequent actions, or it can simply overwhelm an analyst if too many false targets are declared. This article describes the theoretical basis for automated target detection and also characterizes the performance of detectors on real data, indicating departures from theory.

Collection of hyperspectral imagery to support algorithm research, development, and performance assessment is a costly proposition, in part due to the sensor operating costs, but also due to the need to carefully characterize the scenes (i.e., find the ground truth) in which data are collected. Even when a data-collection campaign runs smoothly, and comprehensive ground truth is provided, the result is still a data

set of limited geographical and temporal scope (limited backgrounds, illumination, seasonal variations) with a limited number of targets. Because of the time-consuming and costly nature of data-collection campaigns, and the limited scope of the data collected, simulation and modeling play an important role in augmenting data sets and examining system trade-offs. The fourth article, "Hyperspectral Imaging System Modeling," by John P. Kerekes and Jerrold E. Baum, introduces a statistical model for hyperspectral imaging and describes its use to support a variety of performance predictions and performance trade-offs.

Recent advances in technology have opened the possibility for combining multispectral and hyperspectral imaging techniques with active illumination and range gating. The fifth article, "Active Spectral Imaging," by Melissa L. Nischan, Rose M. Joseph, Justin C. Libby, and John P. Kerekes, describes a research effort to identify applications for—and quantify the performance advantages of—active illumination of scenes in both hyperspectral and multispectral imaging.

Hyperspectral imaging relies primarily on spectral features to detect and identify targets (more precisely, to identify the surface coatings of targets), whereas high-resolution panchromatic imagery and radar imagery rely more on spatially invariant features to detect and identify targets. Each of these sensing modalities has strengths and weaknesses. An important area of research addresses methods for combining or fusing the information from multimodal sensing to improve the overall detection and identification performance against different classes of target. The sixth article, "Multisensor Fusion with Hyperspectral Imaging Data: Detection and Classification," by Su May Hsu and Hsiao-hua K. Burke, describes several methods for fusing spatial and spectral information from heterogeneous sensors to increase detection and identification performance, as well as provide more easily interpretable fused imagery.

Acknowledgments

The authors would like to thank our colleagues Michael Griffin, Jerry Baum, and Peter Boettcher for their contributions to Figures 2, 4, and 9, respectively, and John Kerekes and Don Lencioni for helpful discussions regarding the spectral-spatial trade space. Much of the work reported in this special issue on spectral imaging was funded by the Office of the Deputy Undersecretary of Defense (Science and Technology).

REFERENCES

1. B.D. Seery, D.B. Cramer, C. Stevens, and D. Lencioni, "EO-1: NASA's First New Millennium Earth Orbiting Mission," *SPIE* **2810,** 1996, pp. 4–10.
2. I.J. Allison and E.A. Neil, "Final Report on the TIROS 1 Meteorological Satellite System," NASA Technical Report R-131, Goddard Space Flight Center, Greenbelt, Md., 1962.
3. W.E. Easias, M.R. Abbott, I. Barton, O.B. Brown, J.W. Campbell, K.I. Carder, D.K. Clark, R.H. Evans, F.E. Hoge, H.R. Gordon, W.M. Balch, R. Letelier, and P.J. Minnett, "An Overview of MODIS Capabilities for Ocean Science Observations," *IEEE Trans. Geosci. Remote Sens.* **35** (4), 1998, pp. 1250–1265.
4. S.L. Ustin, D.A. Roberts, and Q.J. Hart, "Seasonal Vegetation Patterns in a California Coastal Savanna Derived from Advanced Visible/Infrared Imaging Spectrometer (AVIRIS) Data," in *Remote Sensing Change Detection: Environmental Monitoring Applications and Methods,* C.D. Elvidge and R.S. Lunetta, eds. (Ann Arbor Press, Ann Arbor, Mich., 1998), pp. 163–180.
5. T. Peli, M. Young, and K. Ellis, "Multispectral Change Detection," *SPIE* **3071,** 1997, pp 97–105.
6. C.A. Wiley, "Pulsed Doppler Radar Methods and Apparatus," U.S. Patent No. 3,196,436, 20 July 1965.
7. S.A. Hovanessian, *Introduction to Synthetic Array and Imaging Radars* (Artech House, Dedham, Mass., 1980).
8. H.A. Zebker and R.M. Goldstein, "Topographic Mapping from Interferometric Synthetic Aperture Radar Observations," *J. Geophys. Res.* **91** (B5), 1986, pp. 4993–4999.
9. D. Landgrebe, "Hyperspectral Image Data Analysis," *IEEE Signal Process. Mag.* **19** (1), 2002, pp. 17–28.
10. D. Landgrebe, "The Evolution of Landsat Data Analysis," *Photogramm. Eng. and Remote Sens.* **LXIII** (7), 1997, pp. 859–867.
11. D.R. Hearn, C.J. Digenis, D.E. Lencioni, J.A. Mendenhall, J.B. Evans, and R.D. Welch, "EO-1 Advanced Land Imager Overview and Spatial Performance," *Proc. IGARRS 2001* **2**, *Sydney, 9–13 2001,* pp. 897–200.
12. G. Vane, "First Results from the Airborne Visible/Infrared Imaging Spectrometer (AVIRIS)," JPL Publication 87-38, 15 Nov. 1987.
13. A.B. Gschwendtner and W.E. Keicher, "Development of Coherent Laser Radar at Lincoln Laboratory," *Linc. Lab. J.* **12** (2), 2000, pp. 383–396.
14. L.J. Rickard, R. Basedow, E. Zalewski, P. Silvergate, and M. Landers, "HYDICE: An Airborne System for Hyperspectral Imaging," *SPIE* **1937,** 1993, pp. 173–179.
15. J. Pearlman, C. Segal, L. Liao, S. Carman, M. Folkman, B. Browne, L. Ong, and S. Ungar, "Development and Operations of the EO-1 Hyperion Imaging Spectrometer," *SPIE* **4135,** 2000, pp. 243–253.

APPENDIX: FUNDAMENTALS OF ATMOSPHERIC COMPENSATION

OVER THE YEARS, MUCH EFFORT has been devoted to methods for quantifying and compensating for the deleterious effects of the atmosphere on spectral imaging, resulting in a variety of atmospheric compensation methods and models. Most of these methods can be classified either as scene-based statistical methods or physics-based modeling methods. The former use *a priori* knowledge of the reflectance characteristics of specific reference objects (such as calibration panels) in a scene to develop statistical relationships between the at-sensor observations and the known surface reflectance. The empirical line method (ELM) is one of the oldest and most commonly used statistical methods for atmospheric compensation [1, 2].

The concept behind the ELM method is simple. Field measurements of the surface reflectance of selected reference objects are made on the ground, at close range, under controlled conditions. These measurements represent ground-truth reflectance data. Typically, the reference objects are carefully selected or constructed to provide relatively constant reflectance over the spectral measurement bands of interest, and they are positioned in the scene to ensure good line-of-sight visibility to the airborne or space-based collection platform. During data collection, these reference objects are included in the imagery collected by the sensor. For each spectral band in the sensor data, a linear regression is performed to relate the raw or calibrated radiance measured in each waveband to the corresponding ground-truth surface reflectance. The result is a gain-offset correction factor for each spectral band.

Figure 1 illustrates the concept for three different spectral bands using HYDICE data containing two reference reflectance objects, one a nominal 4% reflectance panel and the other a nominal 32% reflectance panel. In this figure, the average radiance for all the pixels in a given panel is plotted against the ground-truth reflectance measurement. Note that the gain G and offset L_o vary across the bands. Given a sensor radiance measurement L_s elsewhere in the scene, the reflectance ρ at that location can be estimated, given the gain and offset terms at each waveband, according to the simple formula

$$\rho = \frac{L_s - L_o}{G}.$$

To a first-order approximation, the offset term L_o is equal to the upwelling path radiance that is superimposed on the desired ground-level radiance signal of interest. The gain term is proportional to the two-way atmospheric transmittance modulated by the solar spectral irradiance.

The ELM generally yields good estimates of the scene's surface reflectances, provided the reflectances of the reference objects are accurate and spectrally uniform. However, a deficiency of the ELM is the assumption that the atmospheric conditions observed over the reference objects are the same throughout other parts of the scene. In fact, information pertain-

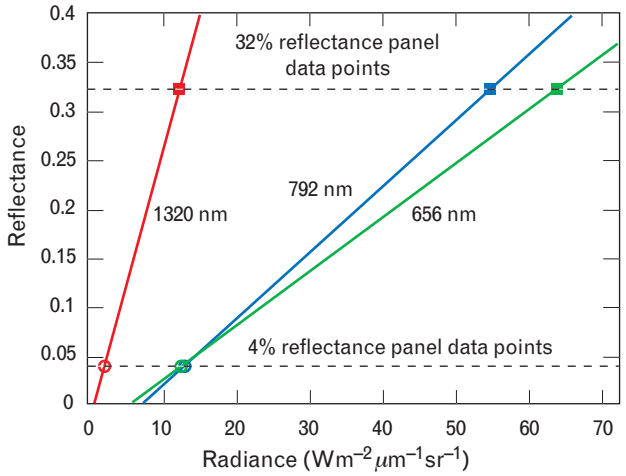

FIGURE 1. Empirical calibration lines for a HYDICE data set from reference reflectance panels positioned in the scene. Three arbitrarily chosen wavelengths illustrate the gain and offset corrections for these bands. The data points defining the lines correspond to two reference panels of 4% and 32% reflectance.

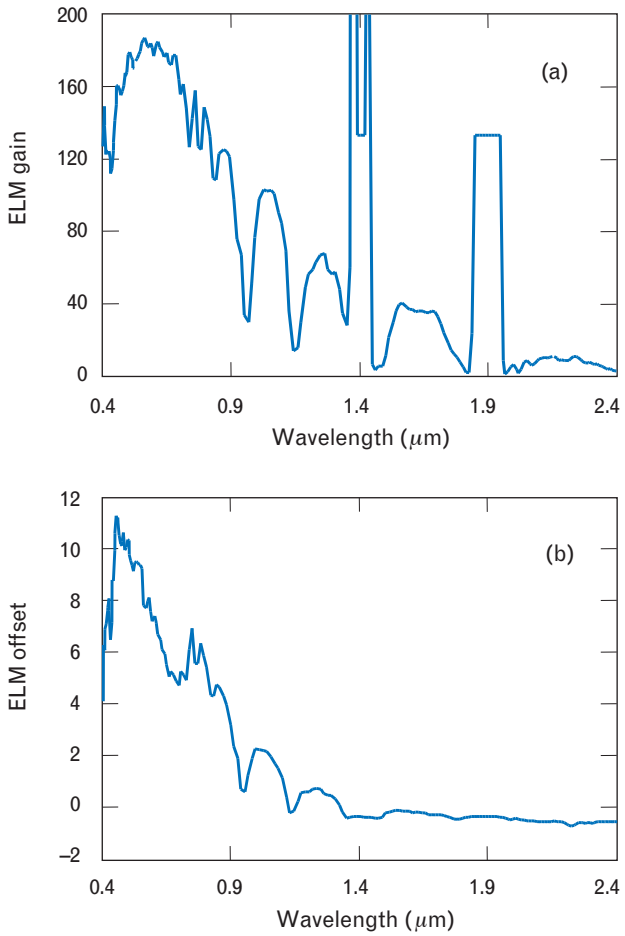

FIGURE 2. Empirical line method (ELM) corrections for (a) gain and (b) offset computed from reference panel reflectances and HYDICE calibrated radiance data.

ing to the intervening atmosphere is not derived with the ELM approach and, consequently, ELM can not account for any variation in the atmosphere across the scene. For example, topographic variations in the atmospheric path result in elevation-dependent residual atmospheric absorptions. An extreme example, but one that is familiar to all, is pockets of fog in low-lying areas, while adjacent areas, at slightly higher elevations, are fog free.

Figure 2 illustrates the ELM gain and offset correction terms, as a function of wavelength, computed for a HYDICE Forest Radiance-I data collection. Note the similarity in shape between the gain correction term of Figure 2(a) and the solar spectral-radiance curve of Figure 2 in the main article. The ELM-derived reflectance obtained by applying the gain and offset correction to the radiance data measured for one of the reference panels is compared to the ground-truth reflectance in Figure 3. Since the ELM gain and offset corrections are derived in part from measurement of the panel, it is not surprising that the fit is good.

When reference panels can't be prepositioned in a scene of interest, methods have been developed to estimate the gain and offset correction terms by using certain naturally occurring objects in the scene. For example, smooth bodies of water usually exhibit very low reflectance, so the radiance measured over such dark objects can be attributed to the upwelling path radiance term L_o. However, dependence upon the presence of suitable reference objects in a scene to perform atmospheric compensation is often limiting. Even if such objects can be found, the implied assumption of atmospheric homogeneity across the scene is often violated. For these reasons, physics-based models have been developed to provide atmospheric compensation even when reference objects of known reflectance are not available.

Two of the more commonly used physics-based models are the atmospheric removal (ATREM) algorithm [3] and fast line-of-sight atmospheric analysis of spectral hypercubes (FLAASH) [4]. While ATREM and FLAASH differ in the details of their approach, both include the key step of using band-ratio techniques [5, 6] to quantify the effects of water

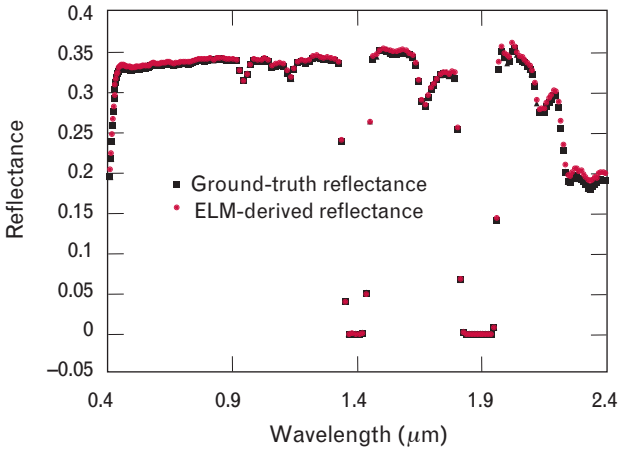

FIGURE 3. ELM-derived reflectance obtained from HYDICE radiance measurements for a 32% reflectance reference panel.

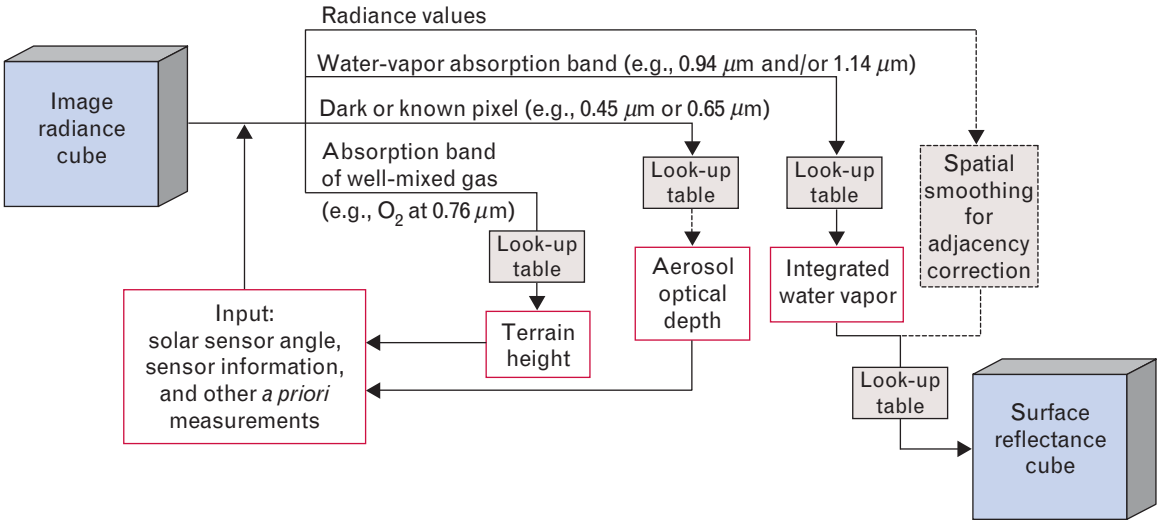

FIGURE 4. Schematic flow of the fast line-of-sight atmospheric analysis of spectral hypercubes (FLAASH) code.

vapor on the hyperspectral measurements. A detailed discussion and comparison of these physics-based atmospheric compensation techniques is beyond the scope of this article, but quantitative evaluations of performance can be found elsewhere [7, 8], including the article in this issue, "Compensation of Hyperspectral Data for Atmospheric Effects," by Michael K. Griffin and Hsiao-hua K. Burke.

In brief, the band-ratio technique involves comparing ratios of radiance measurements made near the edges of known atmospheric water-vapor absorption bands in order to estimate the column water vapor in the atmosphere on a pixel-by-pixel basis. Look-up tables (LUT), indexed by measured quantities in the scene, combined with other specified information such as the solar zenith angle, provide the information necessary to estimate reflectance across the scene, without resorting to reference objects within the scene. Other information in addition to reflectance can also be derived from the physics-based models, including estimates of terrain height and aerosol optical depth (visibility). Figure 4 shows a simplified block diagram of the FLAASH processing flow.

REFERENCES

1. D.D. Roberts, Y. Yamaguchi, and R.P. Lyon, "Calibration of Airborne Imaging Spectrometer Data to Percent Reflectance Using Field Spectral Measurements," *Proc. Nineteenth Int. Symp. on Remote Sensing of Environment* **2**, *Ann Arbor, Mich., 21–25 Oct. 1985,* pp. 679–688.
2. J.E. Conel, R.O. Green, G. Vane, C.J. Bruegge, R.E. Alley, and B.J. Curtiss, "Airborne Imaging Spectrometer-2: Radiometric Spectral Characteristics and Comparison of Ways to Compensate for the Atmosphere," *SPIE* **834**, 1987, pp. 140–157.
3. B.-C. Gao, K.B. Heidebrecht, and A.F.H. Goetz, "Derivation of Scaled Surface Reflectances from AVIRIS Data," *Rem. Sens. Environ.* **44** (2/3), 1993, pp. 165–178.
4. S.M. Adler-Golden, A. Berk, L.S. Bernstein, S. Richtsmeier, P.K. Acharya, M.W. Matthew, G.P. Anderson, C. Allred, L. Jeong, and J. Chetwynd, "FLAASH, A MODTRAN4 Atmospheric Correction Package for Hyperspectral Data Retrievals and Simulations," *Proc. 7th Ann. JPL Airborne Earth Science Workshop*, Pasadena, Calif., 1998, JPL Publication 97-21, pp. 9–14.
5. B.-C. Gao and A.F.H. Goetz, "Column Atmospheric Water Vapor and Vegetation Liquid Water Retrievals from Airborne Imaging Spectrometer Data," *J. Geophys. Res.* **95** (D4), 1990, pp. 3549–3564.
6. B.-C. Gao and Y.J. Kaufman, "The MODIS Near-IR Water Vapor Algorithm, Algorithm Technical Background Doc. ID: MOD05: Total Precipitable Water," NASA Goddard Space Flight Center, Greenbelt, Md., 1997.
7. M.W. Matthew, S.M Adler-Golden, A. Berk, G. Felde, G.P. Anderson, D. Gorodetzkey, S. Paswaters, and M. Shippert, "Atmospheric Correction of Spectral Imagery: Evaluation of the FLAASH Algorithm with AVIRIS Data," *SPIE* **5093**, 2003.
8. M.K. Griffin, H. K. Burke, J. Vail, S.M. Adler-Golden, and M. Matthew, "Sensitivity of Atmospheric Compensation Model Retrievals to Input Parameter Specification," *Proc. AVIRIS Earth Science and Applications Workshop*, Pasadena, Calif., 1999, JPL Publication 99-17.

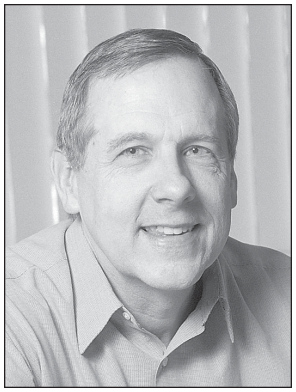

GARY A. SHAW
is a senior staff member in the Advanced Space Systems and Concepts group. His current research focus is on collaborative sensing concepts, including energy-efficient techniques for both line-of-sight and non-line-of-sight electro-optical communication and networking. He joined Lincoln Laboratory in 1980 to work on adaptive processing for radar systems, and was a member of the study team that launched a program in the early 1980s to develop concepts for affordable space radar. From 1984 to 1987 he served as test director and assistant leader of the ALCOR and MMW radars at the Kwajalein Reentry Measurements Site. After his Kwajalein tour he served as assistant group leader and then associate group leader in what is now the Sensor Technology and System Applications Group, where he applied his signal processing expertise to radar and passive sensor algorithm development. He received B.S. and M.S. degrees in electrical engineering from the University of South Florida, and a Ph.D. degree in electrical engineering from the Georgia Institute of Technology, where he was both a President's Fellow and a Schlumberger Fellow.

HSIAO-HUA K. BURKE
is the leader of the Sensor Technology and System Applications group. In the area of remote sensing, she specializes in applications of optical sensors, particularly data analysis and algorithm development. A recent area of interest is the application of hyperspectral technology to the Department of Defense, including fusion of hyperspectral data information with other sensors. She received a Ph.D. degree in atmospheric physics from Rice University, and joined Lincoln Laboratory as a staff member in 1981.